Cardiac conduction is required to preserve cardiac chamber morphology

Neil C. Chi[a,b,c,d,1], Markus Bussen[e], Koroboshka Brand-Arzamendi[a], Chunhua Ding[b], Jeffrey E. Olgin[b,c], Robin M. Shaw[b,c], Gail R. Martin[c,e], and Didier Y. R. Stainier[a,c,1]

Departments of [a]Biochemistry and Biophysics, Programs in Developmental Biology, Genetics and Human Genetics, [e]Anatomy, and [b]Medicine and [c]Cardiovascular Research Institute, University of California, San Francisco, CA 94158; and [d]Department of Medicine, Division of Cardiology, University of California at San Diego, La Jolla, CA 92093-0613J

Edited by Eric N. Olson, University of Texas Southwestern, Dallas, TX, and approved June 22, 2010 (received for review August 19, 2009)

Electrical cardiac forces have been previously hypothesized to play a significant role in cardiac morphogenesis and remodeling. In response to electrical forces, cultured cardiomyocytes rearrange their cytoskeletal structure and modify their gene expression profile. To translate such in vitro data to the intact heart, we used a collection of zebrafish cardiac mutants and transgenics to investigate whether cardiac conduction could influence in vivo cardiac morphogenesis independent of contractile forces. We show that the cardiac mutant *dco*^{s226} develops heart failure and interrupted cardiac morphogenesis following uncoordinated ventricular contraction. Using in vivo optical mapping/calcium imaging, we determined that the *dco* cardiac phenotype was primarily due to aberrant ventricular conduction. Because cardiac contraction and intracardiac hemodynamic forces can also influence cardiac development, we further analyzed the *dco* phenotype in noncontractile hearts and observed that disorganized ventricular conduction could affect cardiomyocyte morphology and subsequent heart morphogenesis in the absence of contraction or flow. By positional cloning, we found that *dco* encodes Gja3/Cx46, a gap junction protein not previously implicated in heart formation or function. Detailed analysis of the mouse *Cx46* mutant revealed the presence of cardiac conduction defects frequently associated with human heart failure. Overall, these in vivo studies indicate that cardiac electrical forces are required to preserve cardiac chamber morphology and may act as a key epigenetic factor in cardiac remodeling.

connexin | development | electrophysiology | genetics | heart

Cardiac morphogenesis is a complex process that is mediated by a coordinated set of cellular and molecular as well as environmental factors (1). Recent studies have shown that epigenetic forces such as cardiomyocyte contractility (2, 3) and intracardiac hemodynamic flow (4) regulate this process. Furthermore, in vitro studies suggest that cardiomyocytes can realign themselves according to electrical conduction directionality (5, 6). However, because electrical cardiac conduction and mechanical contractile forces are intimately coupled in the intact heart, it is difficult to assess the individual contribution of these influences to overall heart organogenesis. Here, we make use of several zebrafish cardiac mutants (7, 8) to uncouple these two influences, and find that electrical conduction exclusive of contractile influences can directly participate in remodeling and morphogenesis of the vertebrate heart.

Results

From a recent ENU mutagenesis screen (8), we identified a zebrafish cardiovascular mutant, *dococ*^{s226} *(dco),* which exhibits asynchronous contraction of the ventricular chamber (compare Movies S1 and S2). The *dco* mutants appear indistinguishable from their WT siblings up to 36–40 h postfertilization (hpf), when the heart is a functional tube. However, at 42–60 hpf, when cardiac chambers are established, *dco* mutants display pericardial edema (Fig. 1*A*). This edema is likely due to dysynchronous ventricular contraction (Fig. 1 *B* and *C;* compare Movies S1 and S2) leading to overall decreased cardiac output and subsequent heart failure. Decreased ventricular myocardial performance in *dco* mutants was further quantified by measuring fractional shortening (Fig. S1).

To understand the molecular nature of the *dco* phenotype, we genetically mapped the *dco*^{s226} mutation to a 0.33cM region on chromosome 9 and identified a mutation in the *connexin48.5* (*cx48.5*) gene (9) (Fig. 1 *D* and *E*). Through protein sequence alignment, phylogenetic and chromosomal synteny analyses, we determined that *cx48.5* is in fact the zebrafish ortholog of *Gja3 (Cx46),* and have thus renamed it zebrafish *cx46* (Fig. S2). Sequence analysis of *dco*^{s226} revealed a missense mutation resulting in a Thr165Ile substitution in a highly conserved amino acid that resides at the pore-forming region in the gap junction M3 transmembrane domain of connexins and has been implicated as a critical amino acid for the function of gap junction channels (10) (Figs. 1 *E* and *F* and S2). In situ expression analysis revealed weak *cx46* expression in zebrafish hearts as early as 36 hpf and stronger expression by 42 hpf (Fig. S3). At 48 and 72 hpf, *cx46* expression appears to be more restricted to the AV canal and ventricle (Fig. S3), a pattern consistent with the observed ventricular conduction phenotype in the mutants. RT-PCR revealed that, in the zebrafish heart, *cx46* is expressed primarily in the myocardium (Fig. S3). Furthermore, knockdown of Cx46 by injection of 1 ng of morpholino (MO) recapitulated the *dco* mutant phenotype (n = 177/203, Fig. S3 and Movie S3). Injection of *cx46* MO into *dco* mutants results in no enhancement or alteration of the mutant phenotype, thus suggesting that the *dco*^{s226} allele is a functional null mutation. Overall, the strong genetic linkage, identification of a molecular lesion in a highly conserved amino acid residue, expression analysis, and MO phenocopy indicate that *cx46* is the gene affected by the *dco* mutation.

Given that gap junction proteins are involved in mediating electrical forces between cardiomyocytes, thereby allowing for coordinate beating of the heart, we hypothesized that the dysynchronous contractions observed in the *dco* mutant hearts might be due to aberrant cardiac conduction rather than a primary contractile defect. Thus, using the *Tg(cmlc2:gCaMP)*^{s878} line, which expresses a calcium-sensitive GFP reporter specifically in the myocardium (8), we performed optical mapping/calcium imaging on *dco* mutant hearts to analyze their cardiac conduction. Because the beating heart can interfere with imaging and analysis of cardiac conduction, this analysis was carried out in the *silent heart*

Author contributions: N.C.C., M.B., and D.Y.R.S. designed research; N.C.C., M.B., K.B.-A., C.D., and R.M.S. performed research; N.C.C., K.B.-A., C.D., and J.E.O. contributed new reagents/analytic tools; N.C.C., M.B., K.B.-A., R.M.S., G.R.M., and D.Y.R.S. analyzed data; and N.C.C., G.R.M., and D.Y.R.S. wrote the paper.

The authors declare no conflict of interest.

This article is a PNAS Direct Submission.

[1]To whom correspondence may be addressed. E-mail: didier.stainier@ucsf.edu or nchi@ucsd.edu.

This article contains supporting information online at www.pnas.org/lookup/suppl/doi:10.1073/pnas.0909432107/-/DCSupplemental.

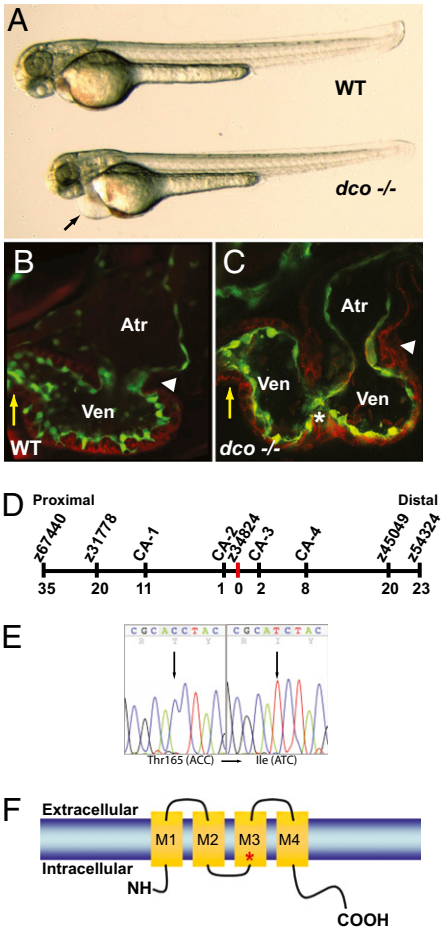

Fig. 1. *dococ*^{s226} Mutants exhibit pericardial edema and cardiac failure due to dysynchronous contraction of the ventricle. (*A*) Brightfield micrographs of 48 hpf WT (WT) and *dco*^{s226} mutant (*dco* $^{-/-}$) embryos. Black arrow points to pericardial edema. (*B* and *C*) Confocal micrographs of 60 hpf *Tg(flk1:EGFP)*^{s843} (*B*) WT and (*C*) *dco*^{s226} mutant hearts (endothelium green) stained with rhodamine phalloidin (myocardium red). *dco* Mutant ventricles fail to contract coordinately and exhibit disorganized chamber walls. White arrowheads point to atrioventricular canal; yellow arrows point to outflow tract; white asterisk denotes aberrant ventricular wall contraction. (*D*) Genetic map of the *dco* region. Numbers below SSLP markers indicate recombination events out of 922 diploid embryos examined. (*E*) Sequencing of *cx46* cDNA revealed a C-to-T change at base pair 494 in the *s226* mutant allele, resulting in a Thr-to-Ile substitution at residue 165. (*F*) Schematic diagram illustrating modular structure of Cx46. A connexon consists of four transmembrane domains (M1–M4). The M3 domain is the major pore-lining domain. Red asterisk marks site affected by *s226* mutation.

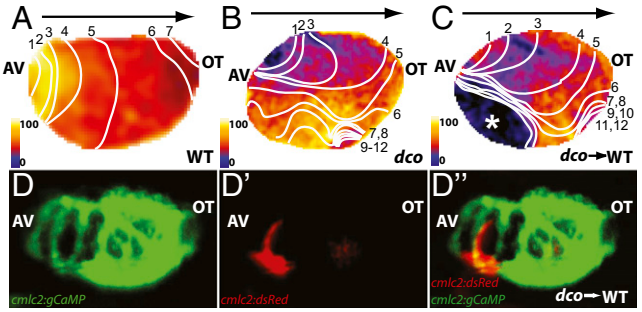

Fig. 2. Optical mapping/calcium imaging of *dococ*^{s226} mutants reveals disrupted cardiac conduction. (*A–C*) Optical maps of calcium excitation during a single cardiac cycle, represented by isochronal lines every 20 ms in 60 hpf embryos carrying the *Tg(cmlc2:gCaMP)*^{s878} reporter and (*A*) WT at the *dco* locus (WT), (*B*) *dco*^{s226} homozygous mutant (*dco*), or (C) WT with *dco*^{s226} mutant cardiomyocytes carrying the *Tg(cmlc2:dsRed)*^{s879} reporter in the ventricle (*dco* → WT). Black arrow shows normal direction of ventricular cardiac conduction. Numbers indicate temporal sequence of calcium excitation. Color bar chart fluorescence intensity changes on a scale of 0 to 100. Cardiac conduction across the WT ventricle proceeds uniformly from the atrioventricular canal (AV) to the outflow tract (OT), whereas cardiac conduction travels aberrantly through the *dco*^{s226} mutant ventricle. Transplanted *dco*^{s226} mutant cardiomyocytes disrupt the organized AV to OT conduction in WT ventricle. White asterisk marks location of transplanted *dco* mutant cardiomyocytes in WT ventricle, as illustrated in *D′* and *D′′*. (*D* and *D′′*) Fluorescent micrographs of the *dco* → WT mosaic heart imaged in *C*. (*D*) Green fluorescence shows the WT host ventricle; (*D′*) donor-derived *dco*^{s226} mutant cardiomyocytes expressing *Tg(cmlc2*:dsRed)^{s879}. (*D′′*) Overlay of green and red fluorescence images reveals that the donor-derived *dco*^{s226} mutant cardiomyocytes are located at the outer curvature of the ventricle near the AV canal, where cardiac conduction is disrupted in the WT host ventricle (*C*).

(*sih*^{b109}) mutant background, which lacks a contracting heart because of a mutation in *tnnt2* (7). Use of *sih* to limit cardiac contraction does not appear to affect the electrical conduction of the heart in the first 4 d of development (7, 8, 11). Optical mapping/calcium imaging of 60 hpf *Tg(cmlc2:gCaMP)*^{s878} *dco;sih* double mutant hearts revealed abnormal conduction throughout the ventricle (compare Fig. 2 *A* and *B*), which is likely responsible for the regional wall motion abnormalities observed in *dco* mutant hearts (Fig. 1*C;* compare Movies S4 and S5).

To gain further insight into the cardiac conduction phenotype, we generated mosaic hearts composed of WT and *dco* mutant cells by transplantation. To facilitate the analysis of these mosaic hearts, we transplanted mutant dsRed/gCaMP-expressing cardiomyocytes into gCaMP-only expressing WT hearts (Fig. 2 *D* and *D′′*). Optical mapping of these mosaic hearts revealed that the presence of mutant *dco* cardiomyocytes disrupted the electrical conduction in WT hearts (Fig. 2*C;* compare Movies S4 and S6). Thus, *dco* mutant cardiomyocytes can affect the electrical conduction in a WT heart. Interestingly, the speed with which the electrical impulse was transmitted through the ventricle (conduction velocity) was also significantly slower in both *dco*$^{-/-}$ and WT/*dco*$^{-/-}$ mosaic ventricles (Fig. 2 *A–C*; compare Fig. 2 *A* and *B*). Given the important role of connexins in communication of electrical signals between cardiomyocytes, it seems likely that lack of Cx46 function leads to failed communication between mutant cells leading to disrupted conduction and dysynchronous contractions of the myocardium. Thus, failed communication between WT and *dco* cardiomyocytes would also lead to disruption of cardiac conduction in the mosaic hearts.

To further investigate the etiology of the dysmorphic *dco* mutant heart, we analyzed *dco* mutants in a combination of mutant and transgenic backgrounds. The cardiac chambers can be divided into three major regions whose morphogenesis is mediated by a multitude of factors. These regions are the outer curvature/OC (the greater, convex curvature of the cardiac chamber), the inner curvature/IC (the lesser, concave curvature of the cardiac chamber), and the atrioventricular canal/AV (the region between the atrial and ventricular chambers) (2, 8) (Fig. 3*A*, yellow-, orange-, and red-outlined regions of the heart, respectively). Using the *Tg(cmlc2:eGFP-ras)*^{s883} line (8, 12), which outlines individual cardiomyocytes with membrane-bound GFP, we further analyzed the cellular characteristics of WT and mutant hearts by confocal microscopy.

Examination of the surface of WT ventricular cardiomyocytes revealed that OC and AV cardiomyocytes are elongated, whereas IC cardiomyocytes are round (Fig. 3 *A* and *F*), as previously reported (2, 8). However, the morphology of *dco*$^{-/-}$ ventricular cardiomyocytes appeared significantly altered compared with WT and was correlated with loss of AV canal constriction and a dysmorphic ventricle (Fig. 3 *B* and *F*). Specifically, mutant OC and

DEVELOPMENTAL BIOLOGY

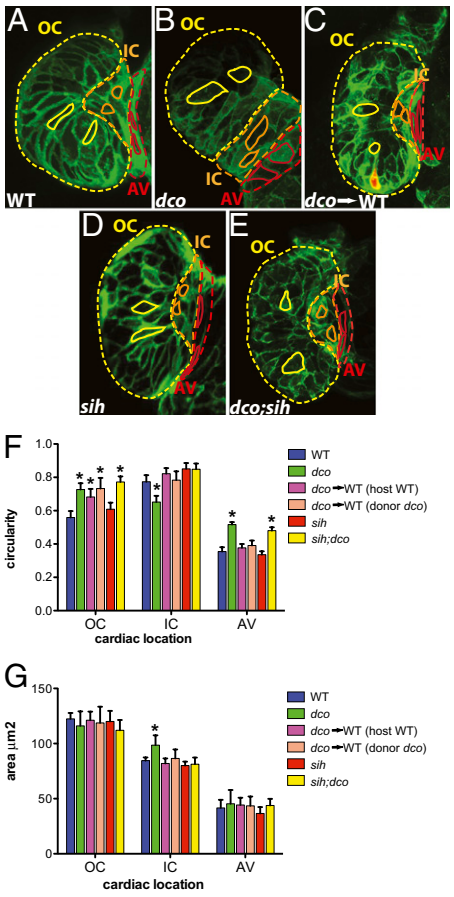

Fig. 3. Cardiac conduction, independent of hemodynamic flow or cardiac contraction, is required for cardiomyocyte morphogenesis. (*A–E*) Confocal images of 60 hpf embryos carrying the *Tg(cmlc2:ras-eGFP)*^{s883} reporter and (A) WT at the *dco* locus (WT), (*B*) *dco*^{s226} homozygous mutant (*dco*), (*C*) WT with *dco*^{s226} mutant cardiomyocytes carrying the *Tg(cmlc2:dsRed)*^{s879} reporter in the ventricle (*dco* → WT), (*D*) *sih* homozygous mutant (*sih*), or (*E*) *dco;sih* double homozygous mutant (*dco;sih*). Outer curvature (OC), inner curvature (IC), and atrioventricular canal (AV) are outlined in yellow, orange, and red dashed lines, respectively. Representative cardiomyocyte shapes for each area are outlined with solid lines. Bar graphs represent (*F*) cell morphology/circularity and (*G*) surface area measurements of *Tg(cmlc2:ras-eGFP)*^{s883} cardiomyocytes at 60 hpf from the outer and inner curvatures of the ventricle as well as the AV canal. Bar height indicates mean for a dataset; error bars indicate SE. *Statistically significant differences compared with WT ($P < 0.001$). Defects in electrical conduction result in aberrant cardiomyocyte morphogenesis.

AV cardiomyocytes appeared more round, whereas IC cardiomyocytes were more elongated compared with WT (Fig. 3 *B* and *F*). In addition, the average surface area of *dco* IC cardiomyocytes was larger than that of WT (Fig. 3*G*).

To further elucidate how *dco* may influence cardiomyocyte morphology, we generated mosaic hearts composed of WT and *dco* mutant cells by transplantation. To facilitate the analysis of these mosaic hearts, we transplanted mutant dsRed/eGFP-ras expressing cardiomyocytes into WT hearts expressing eGFP-ras only (Fig. 3*C*). Because transplanted *dco*$^{-/-}$ cardiomyocytes were randomly distributed within the WT host ventricle, cardiomyocyte morphologic phenotypes were more variable. Furthermore, the disruption of organized ventricular conduction and wall contraction was dependent on the number of transplanted *dco*$^{-/-}$ cardiomyocytes. For example, greater numbers of mutant donor cardiomyocytes resulted in greater disruption of synchronized ventricular conduction and wall contraction. Nevertheless, in mosaic hearts, both donor *dco*$^{-/-}$ and WT host OC cardiomyocytes exhibited, on average, more circular shapes compared with cardiomyocytes of WT-only hearts (Fig. 3*F* and compare Fig. 3*A* and 3*C*), whereas donor *dco*$^{-/-}$ and WT host IC cardiomyocytes appeared less elongated compared with cardiomyocytes of *dco*$^{-/-}$ only hearts (Fig. 3*F* and compare Fig. 3*B* with 3*C*).

Because these cell shape changes might be due to uncoordinated contractions of the ventricle as contractile forces can influence cell morphology (2), we analyzed cardiac morphogenesis in noncontracting *dco* mutant hearts to determine whether electrical forces could independently affect cardiac morphogenesis. We observed that *sih*$^{-/-}$ ventricular cardiomyocytes, which exhibit normal electrical conduction, were not significantly different from WT (Fig. 3 *D* and *F*). However, in the absence of cardiac contraction in the *dco;sih* double mutant ventricles, we found that disorganized ventricular conduction due to the *dco* mutation resulted in deformed AV and OC cardiomyocytes (Fig. 3 *E* and *F*). Interestingly, *dco;sih* double mutant IC cardiomyocytes did not appear to be as affected as *dco*$^{-/-}$ mutant IC cardiomyocytes. This difference may be due to aberrant contractile forces having a greater influence on the inner curvature of the ventricle than aberrant conduction. Thus, these findings provide in vivo evidence that electrical forces can have an impact on the morphology of growing/elongating OC and AV cardiomyocytes, and may be necessary for overall morphogenesis of the heart. Furthermore, although AV canal and chamber formation begins at ~37–45 hpf (13) and milder *dco*$^{-/-}$ cardiomyocyte phenotypes were observed at 45–48 hpf, these defects were most pronounced by 60 hpf, suggesting that the influence of electrical forces on cell morphology may accrue over time.

To evaluate whether Cx46 could restore proper ventricular conduction, we attempted to rescue the *dco*^{s226} mutant cardiac phenotype with injection of zebrafish and mouse *Cx46* mRNA as well as with cardiac specific expression of zebrafish *cx46* (Fig. 4). After injecting WT zebrafish *cx46* mRNA, ~56% of *dco*^{s226} mutant hearts exhibited complete rescue of ventricular conduction and contraction (n = 35/62), whereas injections of zebrafish *cx46*^{s226} mRNA failed to rescue (n = 0/60) (Fig. 4C and Table S1). Myocardial specific expression of a WT zebrafish *cx46* transgene (*Tg(cmlc2:cx46-eGFP*^{s882}*)*) rescued 100% of the *dco*^{s226} mutants (n = 74/74), whereas myocardial specific expression of a zebrafish *cx46*^{s226} transgene [*Tg(cmlc2:cx46mt-eGFP*^{s925}*)*] did not (n = 0/67) (Fig. *4 A–C* and Table S1). The ventricular conduction defects are not likely caused by defects in cardiomyocyte Cx46 trafficking, as mutant Cx46-GFP fusion protein localized to the cell membrane similar to WT Cx46-GFP fusion protein (Fig. 4 *A* and *B*). In addition, injection of the murine *Cx46* mRNA rescued ~25% of *dco*^{s226} mutant hearts (n = 15/59), illustrating the functional conservation of Cx46 (Fig. 4*C* and Table S1). However, injection of zebrafish *cx43* mRNA, which encodes a connexin highly abundant in vertebrate hearts, did not rescue the *dco* conduction phenotype (n = 0/55), illustrating the specificity of Cx46 in mediating cardiac conduction (Fig. 4*C* and Table S1). Interestingly, mRNA injection (n = 24/168) or myocardial specific expression (n = 16/188) of a zebrafish *cx46*^{s226} transgene (*Tg(cmlc2:cx46mt-eGFP*^{s925}*)*) induced the *dco* phenotype in some WT hearts, suggesting that zebrafish Cx46^{s226} at high enough levels can act as a dominant negative inhibitor of WT Cx46 (Fig. 4*D* and Table S1).

To test whether the functional role of CX46 is conserved between zebrafish and mammals, we analyzed mice carrying a *Cx46* null allele created by replacing vital coding sequences with a *lacZ* gene (*Cx46*^{lacZ}) (14). In neonatal *Cx46*$^{lacZ/+}$ mouse hearts, lacZ positive cells were detected in the atrium, subendocardial region of the ventricle, atrioventricular canal and the interventricular septum where the His bundle branch fibers reside (Fig. 5 *A* and *B*). Furthermore, we found that by in situ hybridization, this lacZ expression recapitulated that of the endogenous *Cx46* gene (Fig. 5*C*). Interestingly, this expression pattern is similar to that ob-

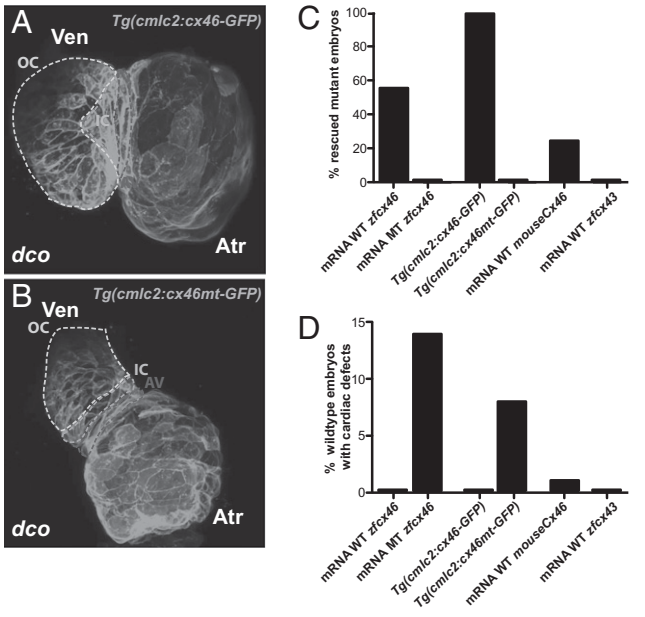

Fig. 4. *dco* Cardiac phenotype is rescued by RNA injection of *Cx46* orthologs as well as by myocardial specific expression of zebrafish *cx46*. (*A* and *B*) Myocardial specific expression of WT [*Tg(cmlc2:cx46-GFP^{s882})*] and mutant [*Tg(cmlc2:cx46mt-GFP^{s925})*] zebrafish Cx46-GFP fusion proteins lead to cell membrane enrichment. Outer curvature (OC), inner curvature (IC), and atrioventricular canal (AV) are outlined by dashed lines. Atr, atrium; Ven, ventricle. (*C*) Injection of WT zebrafish (WT *zfcx46*) or mouse *Cx46* (mouse*Cx46*) mRNA as well as myocardial specific expression of WT zebrafish Cx46-GFP fusion proteins [*Tg(cmlc2:cx46-GFP^{s882})*] rescued the *dco* cardiac phenotype. On the other hand, injection of zebrafish *cx46^{s226}* (MT *zfcx46*) or *cx43* (*zfcx43*) mRNA as well as myocardial specific expression of zebrafish Cx46^{s226}-GFP [*Tg(cmlc2:cx46mt-GFP^{s925})*] failed to rescue the *dco* cardiac phenotype. (*D*) However, injection of zebrafish *cx46^{s226}* mRNA or myocardial specific expression of zebrafish Cx46^{s226}-GFP [*Tg(cmlc2:cx46mt-GFP^{s925})*] in WT embryos resulted in *dco* cardiac phenotypes. In addition, RNA overexpression of WT murine *Cx46* caused a *dco* cardiac phenotype in a small percentage of WT embryos.

served for the cardiac conduction system (15). To determine whether loss of Cx46 function affects cardiac conduction, we performed surface electrocardiograms (ECGs) in WT and mutant littermates (Fig. 5 *D* and *E* and Table S2). The average heart rate in *Cx46$^{lacZ/lacZ}$* (null) mice was significantly lower than that of their WT littermates (Fig. 5*F*). In addition, ventricular depolarization was significantly prolonged in the mutant hearts, as manifested by a QRS and QT prolongation, increased width of the S wave and the rsR′ complex (Fig. 5 *D* and *E* and Table S2). Synchronous depolarization of the ventricular cardiomyocytes is coordinated by rapid conduction through the atrioventricular node/His-Purkinje system. The morphology and widening of the QRS complex in the *Cx46* mutants are typical of aberrant conduction along the His bundle branches (bundle branch block), where *Cx46* expression was detected. These electrical findings observed in the *Cx46$^{lacZ/lacZ}$* (null) mice are functionally similar to those observed in the *dco* zebrafish mutant; that is, both mouse and zebrafish *Cx46* mutant hearts exhibit a similar defect in cardiac conduction from the AV canal to the ventricle. Furthermore, *Cx46* appears to be expressed in the AV myocardium in both mouse and zebrafish hearts. Although zebrafish hearts do not possess an interventricular septum, *cx46* appears to be expressed within specific ventricular cardiomyocytes, which may be the functional equivalent to the mammalian His-Purkinje where mouse *Cx46* is also expressed. In contrast to the *dco* mutant, the *Cx46$^{lacZ/lacZ}$* (null) mice are viable and do not exhibit obvious cardiac morphologic phenotypes. This difference in viability as well as cardiac morphology and function may be due to functional redundancy with additional connexins (Cx40 and Cx45) expressed in the mouse His bundle branches (16, 17). Interestingly, the electrical phenotypes of the mouse *Cx46* mutant are commonly associated with adult human ventricular dyssynchrony and heart failure, and thus it may become informative to examine more closely the various SNPs present in the human *CX46* gene.

Discussion

The direction of growth and orientation of various cell types in tissue culture can be influenced by externally applied electric fields (18, 19). Furthermore, endogenous electric currents exist in a variety of tissues and have been hypothesized to influence cell migration and shape (20). However, whether these natural currents can generate electric fields sufficient to direct organogenesis in vivo remains unclear. Our in vivo results indicate that physiologic electric currents can indeed have an impact on cell morphology and overall cardiac organogenesis.

These electrical effects might be mediated through intracellular calcium fluxes which can affect cell polarization (21, 22). Furthermore, a number of cell surface receptors, including receptors for Con A (23), Acetycholine (24), and Fc (25) can also be redistributed in the cell membrane by electric fields. Cadherins, cell surface adhesion molecules that mediate calcium-dependent homophilic cell–cell contact, typically confer strong adhesion between cells when they are anchored to the cytoskeleton through their cytoplasmic binding partners (26, 27). Previous studies have revealed that the distribution of N-cadherin can be changed through physiologic depolarization of synapses (28). In addition, recent in vitro findings have shown the involvement of calcium and integrins in directional responses of zebrafish keratocytes to electric fields (29). Thus, it is possible that disrupted cardiac conduction leading to changes in the intracellular calcium gradients, as revealed by the optical mapping/calcium imaging of the mutant zebrafish hearts (Fig. 2), results in redistribution of integrins or N-cadherin, a cadherin specifically expressed in the myocardium. As a result, mislocalization of these adhesion molecules could lead to loss of cell–cell contact between cardiomyocytes and could affect cell shapes and overall cardiac morphogenesis.

These results also suggest that primary cardiac conduction disorders could directly lead to aberrant remodeling of the heart and reduced cardiac systolic function. Thus, overall cardiac improvement from the resynchronization of the ventricles in heart failure patients manifesting conduction disorders (30, 31) may be due to beneficial realignment and improved remodeling of the myocardium primarily from proper and synchronized electrical signaling. Recent findings have also revealed a reduction in postinfarct arrhythmias from electrical cell–cell communication of engrafted embryonic cardiomyocytes and skeletal myoblasts to injured myocardium (32). Given that previous cardiac cell-based therapy has provided only a modest improvement in cardiac function, electrical cell–cell communication and stimulation may be required for optimal integration and alignment of engrafted embryonic cardiomyocytes and skeletal myoblasts in the injured myocardium to improve overall myocardial performance.

Materials and Methods

Zebrafish Strains. Embryos and adult fish were raised and maintained under standard laboratory conditions. We used the following lines: *dco^{s226}* (8), *Tg(cmlc2:gfp)^{s883}* (12), *Tg(cmlc2:gCaMP)^{s878}* (8), *Tg(cmlc2:dsRed)^{s879}* (8), *Tg(cmlc2:eGFP-ras)^{s883}* (8), *Tg(cmlc2:cx46-eGFP)^{s882}*, *Tg(kdrl:HsHRAS-mcherry)^{s896}* (12), and *Tg(cmlc2:cx46mt-eGFP)^{s925}*.

Mapping. We mapped the *dco* mutation to linkage group 9 using a set of SSLP markers. For fine mapping, 922 mutant embryos were tested with SSLP markers in the critical interval (Fig. 1*D*). *cx46/gja3* cDNA was isolated, sequenced, and analyzed from *s226* mutant embryos and their WT siblings.

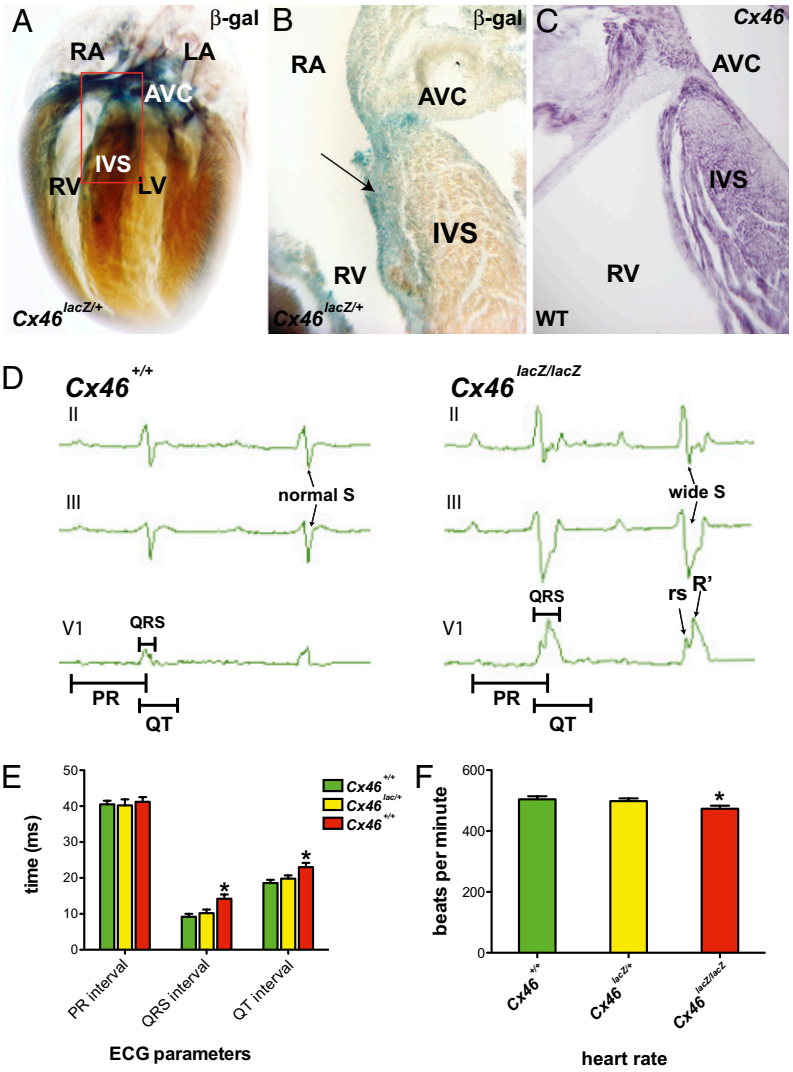

Fig. 5. Murine *Cx46* is expressed in the fast cardiac conduction system, and its disruption results in cardiac conduction defects. (*A*) Whole-mount β-gal staining of $Cx46^{lacZ/+}$ postnatal mice (P3). $Cx46^{lacZ/+}$ cells are detected in the atrium, ventricle, atrioventricular canal (AVC), and interventricular septum (IVS). Red box outlines the IVS and AVC regions. (*B*) Section analysis of region outlined by red box in *A* containing IVS and AVC reveals $Cx46^{lacZ/+}$ cells in subendocardium of IVS where His-Purkinje fibers reside (black arrow). (*C*) Section RNA in situ hybridization of endogenous *Cx46* expression in WT CD1 P3 mice is consistent with X-gal staining of $Cx46^{lacZ/+}$ cardiac tissue. (*D*) Representative three-lead electrocardiogram (ECG) recordings from WT and $Cx46^{lacZ/lacZ}$ (null) mice. *Cx46* null ECGs exhibited prolonged QRS and QT intervals, suggesting an intraventricular conduction delay. *Cx46* null ECGs also exhibited an rSR′ morphology in lead V1 and a wide S wave in leads II and III, indicating uncoordinated ventricular activation. Bar graphs represent (*E*) ECG measurements (PR, QRS intervals, and QT), and (*F*) heart rate of $Cx46^{+/+}$, $Cx46^{lacZ/+}$, and $Cx46^{lacZ/lacZ}$ hearts. Bar height indicates mean for datasets; error bars indicate SE (Table S2). *Statistically significant differences between phenotypically WT ($Cx46^{+/+}$ and $Cx46^{lacZ/+}$) and mutant ($Cx46^{lacZ/lacZ}$) hearts ($P < 0.05$). LA, left atrium; LV, left ventricle; RA, right atrium; RV, right ventricle.

Immunohistochemistry, Confocal Microscopy, Cell Morphology, in Situ Analysis, and RT-PCR. Whole-mount in situ hybridization was performed on 24, 30, 36, 42, 48, and 72 hpf zebrafish embryos as previously described (8), using the *cx46* probe. The *cx46 in situ* probe was generated by PCR amplification from the 3′ end of the gene using the following primers: *cx46* zebrafish F: atttcccggcctacagaaaagac; *cx46* zebrafish R: gcaatctgcctctcacttcctct. *cx46* RT-PCR experiment was performed from RNA obtained from FACS sorted myocardial (green fluorescence) and endocardial (red fluorescence) cells of isolated *Tg(cmlc2:gfp);Tg(kdrl:HsHRAS-mcherry)* 48 hpf hearts. Primer sequences used for RT-PCR are the following: *cx46* – F 5′ tgcctgaggcggacgaagctgagc 3′; R 5′ gctttgaggtgcagagccactaca 3′ and β-actin1–F 5′ cgtctggatctggctggtcgtgacc 3′; and R 5′ ctcatcgtactcctgcttgctgat 3′. Immunohistochemistry, confocal microscopy, and live imaging of zebrafish hearts were performed as previously described (8). Cardiomyocyte surfaces and cross-sections were analyzed from hearts captured by live confocal imaging using ImageJ software (National Institutes of Health; http:rsb.info.hin.gov/ij/) as described previously (2, 8). Only cells with clearly visible outlines were measured in the xy plane of view. Because the curvatures of some cardiomyocytes were distorted in mutant embryos, we processed images to focus these cardiomyocytes in the xy focal plane. Furthermore, we compared pooled circularity and surface area data obtained from outer curvature (OC), inner curvature (IC), and atrioventricular (AV) WT and mutant ventricular cardiomyocytes. Cardiomyocytes were measured in 12 WT (149 OC, 98 IC, and 58 AV cells), 12 $sih^{-/-}$ (155 OC, 106 IC, and 69 AV cells), 14 $dco^{-/-}$ (171 OC, 119 IC, and 78 AV cells), 16 $dco^{-/-}$;$sih^{-/-}$ (203 OC, 132 IC, and 97 AV cells), and 8 $dco^{-/-}$ to WT transplant (OC, 23 $dco^{-/-}$/85 WT; IC, 14 $dco^{-/-}$/57 WT; and AV, 10 $dco^{-/-}$/39 WT cells) embryonic hearts. Circularity measurements discriminate circular cells (circularity = 1) from elliptical cells (circularity <1).

Video Recording/Microscopy. Brightfield pictures and videos were taken using a Stemi SV11 dissecting microscope (Zeiss). Videos were captured using a standard CCD camera at 20 frames/s.

Physiology Analysis: Optical Mapping of Cardiac Conduction and Measurement of Cardiac Output. Optical mapping/calcium imaging analysis was performed on individual zebrafish between 48 and 72 hpf. Motion artifact was suppressed in all optical mapping experiments using the *sih* mutant (7). Images

were acquired and data analysis performed as previously described (8). To calculate fractional shortening, end-diastolic (EDD) and end-systolic diameter (ESD) were measured from time-lapse videos of a lateral view of a beating heart. Fractional shortening = (EDD − ESD)/EDD. Cardiac output was measured as previously described (33).

Morpholino Knockdown and mRNA/Transgenic Rescue Experiments. To knock down the translation of zebrafish *cx46*, we used a morpholino oligonucleotide targeted against an ATG upstream of the translational start site of *cx46/gja3* with the following sequence: 5′-GCTTCACGATTTCTAGCCTAGAGAG-3′. Embryos were injected at the one-cell stage with 1 ng *cx46/gja3* morpholino and assessed between 40 and 48 hpf. For mRNA rescue experiments, one-cell stage embryos were injected with 50–150 pg zebrafish WT or mutant *cx46/gja3,* mouse WT *Cx46*, or zebrafish *cx43* mRNA. Zebrafish myocardial-specific *cx46* rescue experiments were performed by crossing either *Tg(cmlc2:cx46-eGFP^{s882})* or *Tg(cmlc2:cx46mt-eGFP^{s925})* into the *dco* mutant background. Brightfield microscopy was used to determine whether the experimental embryos exhibited the *dco* aberrant or WT organized conduction and contraction.

Transplantations. Cell transplantations were performed at midblastula stages as previously described (34). Twenty to 30 cells were transplanted from *dco* embryos carrying either *Tg(cmlc2:dsRed);Tg(cmlc2:gCaMP)* or *Tg(cmlc2:dsRed);Tg(cmlc2:eGFP-ras)* into the margin of WT host embryos carrying *Tg(cmlc2:gCaMP)* or *Tg(cmlc2:eGFP-ras)*, respectively. In all, 22 of 163 (13.5%) transplants successfully donated *dco;Tg(cmlc2:dsRed);Tg(cmlc2:gCaMP)* myocardial cells into WT *Tg(cmlc2:gCaMP)* host embryos. Of 121 transplants, 17 (14.1%) transplants successfully donated *dco;Tg(cmlc2:dsRed);Tg(cmlc2:eGFP-ras)* myocardial cells into WT *Tg(cmlc2:eGFP-ras)* host embryos.

Mouse *Cx46* in Situ Hybridization. A mouse *Cx46* probe was amplified from 2-d-old mouse heart cDNA using the following primers: *Cx46* mouseF1: tgacgacagagcagaactggac; *Cx46* mouseR1: ttcatcatgacagaatagtggagga. RNA in situ hybridization was performed according to standard protocols on paraffin-embedded, 3-d-old WT hearts sectioned into 10-μm-thick slices.

Connexin46$^{lacZ/+}$ Stainings. *Cx46$^{lacZ/+}$* postnatal day 3 (P3) mice were used to study the expression of the β-galactosidase reporter gene. *Cx46$^{lacZ/+}$* hearts were isolated and fixed for 1 h in PBS containing 2% formaldehyde and 0.05% glutaraldehyde on ice. The hearts then were extensively rinsed in PBS containing 0.01% sodium desoxycholate, 0.02% Nonidet P-40, 2 mM $MgCl_2$, and 2 mM EGTA. X-gal staining was carried out in rinsing solution containing 0.5 mg/mL X-gal, 10 mM $K_3Fe(CN)_6$, and 10 mM $K_4Fe(CN)_6$ at 37 °C for at least 24 h. For whole-mount expression analysis, the hearts were dehydrated through an alcohol series and then cleared in benzyl aldehyde/benzyl benzoate (BABB). X-Gal stained *Cx46$^{lacZ/+}$* hearts were also sectioned.

Electrocardiography. For surface electrocardiography, mice were anesthetized. Four-needle electrodes were placed subcutaneously in standard limb lead configurations and one in the precordial V1 lead position. For each mouse, 10–20 s of continuous signals were sampled in each lead configuration. Data analysis was performed using electronic calipers on averaged beats (Spike 2; Cambridge Electronic Design). The QRS interval was measured from the onset of the Q-wave to the isoelectric point preceding the first, rapid repolarization wave. The QT interval was measured from the onset of the Q-wave to the end of the second, slower repolarization wave. The measured QT interval was corrected for heart rate.

ACKNOWLEDGMENTS. We thank Ana Ayala and Milagritos Alva for expert help with the fish and Xiaohua Gong (University of California, Berkeley, CA) for generously providing the *Gja3/Cx46* mutant mouse. This work was supported by National, Heart, Lung and Blood Institute Grants HL074891 and HL094414 (to N.C.C. and R.M.S.); by GlaxoSmithKline Research and Education Foundation Cardiovascular Awards and Fellow to Faculty American Heart Association postdoctoral awards (to N.C.C. and R.M.S.); by National Institutes of Health Grant HD25331 (to G.R.M.); and by the Packard Foundation and National Institutes of Health Grant HL54737 (to D.Y.R.S.).

1. Olson EN (2006) Gene regulatory networks in the evolution and development of the heart. *Science* 313:1922–1927.
2. Auman HJ, et al. (2007) Functional modulation of cardiac form through regionally confined cell shape changes. *PLoS Biol* 5:e53.
3. Bartman T, et al. (2004) Early myocardial function affects endocardial cushion development in zebrafish. *PLoS Biol* 2:E129.
4. Hove JR, et al. (2003) Intracardiac fluid forces are an essential epigenetic factor for embryonic cardiogenesis. *Nature* 421:172–177.
5. Radisic M, et al. (2004) Functional assembly of engineered myocardium by electrical stimulation of cardiac myocytes cultured on scaffolds. *Proc Natl Acad Sci USA* 101: 18129–18134.
6. Tung L, Sliz N, Mulligan MR (1991) Influence of electrical axis of stimulation on excitation of cardiac muscle cells. *Circ Res* 69:722–730.
7. Sehnert AJ, et al. (2002) Cardiac troponin T is essential in sarcomere assembly and cardiac contractility. *Nat Genet* 31:106–110.
8. Chi NC, et al. (2008) Genetic and physiologic dissection of the vertebrate cardiac conduction system. *PLoS Biol* 6:e109.
9. Cheng S, Shakespeare T, Mui R, White TW, Valdimarsson G (2004) Connexin 48.5 is required for normal cardiovascular function and lens development in zebrafish embryos. *J Biol Chem* 279:36993–37003.
10. Skerrett IM, et al. (2002) Identification of amino acid residues lining the pore of a gap junction channel. *J Cell Biol* 159:349–360.
11. Milan DJ, Giokas AC, Serluca FC, Peterson RT, MacRae CA (2006) Notch1b and neuregulin are required for specification of central cardiac conduction tissue. *Development* 133:1125–1132.
12. Chi NC, et al. (2008) Foxn4 directly regulates tbx2b expression and atrioventricular canal formation. *Genes Dev* 22:734–739.
13. Walsh EC, Stainier DY (2001) UDP-glucose dehydrogenase required for cardiac valve formation in zebrafish. *Science* 293:1670–1673.
14. Gong X, et al. (1997) Disruption of alpha3 connexin gene leads to proteolysis and cataractogenesis in mice. *Cell* 91:833–843.
15. Mikawa T, Hurtado R (2007) Development of the cardiac conduction system. *Semin Cell Dev Biol* 18:90–100.
16. Davis LM, Kanter HL, Beyer EC, Saffitz JE (1994) Distinct gap junction protein phenotypes in cardiac tissues with disparate conduction properties. *J Am Coll Cardiol* 24:1124–1132.
17. Jalife J, Morley GE, Vaidya D (1999) Connexins and impulse propagation in the mouse heart. *J Cardiovasc Electrophysiol* 10:1649–1663.
18. Jaffe LF, Nuccitelli R (1977) Electrical controls of development. *Annu Rev Biophys Bioeng* 6:445–476.
19. Luther PW, Peng HB, Lin JJ (1983) Changes in cell shape and actin distribution induced by constant electric fields. *Nature* 303:61–64.
20. Jaffe LF, Stern CD (1979) Strong electrical currents leave the primitive streak of chick embryos. *Science* 206:569–571.
21. Robinson KR (1985) The responses of cells to electrical fields: A review. *J Cell Biol* 101: 2023–2027.
22. Wei C, et al. (2009) Calcium flickers steer cell migration. *Nature* 457:901–905.
23. Poo M, Robinson KR (1977) Electrophoresis of concanavalin A receptors along embryonic muscle cell membrane. *Nature* 265:602–605.
24. Orida N, Poo MM (1978) Electrophoretic movement and localisation of acetylcholine receptors in the embryonic muscle cell membrane. *Nature* 275:31–35.
25. McCloskey MA, Liu ZY, Poo MM (1984) Lateral electromigration and diffusion of Fc epsilon receptors on rat basophilic leukemia cells: Effects of IgE binding. *J Cell Biol* 99: 778–787.
26. Takeichi M (1991) Cadherin cell adhesion receptors as a morphogenetic regulator. *Science* 251:1451–1455.
27. Meng W, Mushika Y, Ichii T, Takeichi M (2008) Anchorage of microtubule minus ends to adherens junctions regulates epithelial cell-cell contacts. *Cell* 135:948–959.
28. Tanaka H, et al. (2000) Molecular modification of N-cadherin in response to synaptic activity. *Neuron* 25:93–107.
29. Huang L, Cormie P, Messerli MA, Robinson KR (2009) The involvement of Ca2+ and integrins in directional responses of zebrafish keratocytes to electric fields. *J Cell Physiol* 219(1):162–172.
30. Bristow MR, et al. Comparison of Medical Therapy, Pacing, and Defibrillation in Heart Failure (COMPANION) Investigators (2004) Cardiac-resynchronization therapy with or without an implantable defibrillator in advanced chronic heart failure. *N Engl J Med* 350:2140–2150.
31. Cleland JG, et al. Cardiac Resynchronization-Heart Failure (CARE-HF) Study Investigators (2005) The effect of cardiac resynchronization on morbidity and mortality in heart failure. *N Engl J Med* 352:1539–1549.
32. Roell W, et al. (2007) Engraftment of connexin 43-expressing cells prevents post-infarct arrhythmia. *Nature* 450:819–824.
33. Bagatto B, Francl J, Liu B, Liu Q (2006) Cadherin2 (N-cadherin) plays an essential role in zebrafish cardiovascular development. *BMC Dev Biol* 6:23.
34. Chung WS, Stainier DY (2008) Intra-endodermal interactions are required for pancreatic beta cell induction. *Dev Cell* 14:582–593.